Materials Advances

ROYAL SOCIETY OF CHEMISTRY

COMMUNICATION

View Article Online
View Journal | View Issue

Cite this: *Mater. Adv.*, 2021, 2, 688

Received 13th October 2020,
Accepted 10th December 2020

DOI: 10.1039/d0ma00793e

rsc.li/materials-advances

Manganese dioxide nanosheet coated carbon cloth as a multifunctional interlayer for advanced lithium–sulfur batteries†

Huayun Liu, Hao Cheng, Han Jin, Cheng Gao, Peng Zhang* and Miao Wang *

Carbonized cotton cloth decorated with manganese dioxide (MnO_2) nanosheets is developed as a multifunctional interlayer. MnO_2 and conductive carbon cloth exhibit dual functions for better electrochemical capability; the batteries with MCC–PP deliver an initial discharge capacity of 843.4 mA h g^{-1} at 1 C with a capacity decay of 0.063% per cycle after 300 cycles.

Lithium–sulfur (Li–S) batteries are expected to be a promising substitute for rechargeable lithium-ion batteries due to their high theoretical specific capacity (1675 mA h g^{-1}) and energy density (2600 W h Kg^{-1}),[1] as well as environmentally friendly feature and lower cost. However, there are still some challenges that hinder the implementation of lithium–sulfur batteries. Typically, these problems mainly revolve around the sulfur cathode in three aspects: (1) lithium polysulfide intermediates inevitably dissolve in the electrolyte, which can result in a serious "shuttle effect";[2] (2) nearly non-conductive sulfur (S) and lithium sulfide (Li_2S) constantly lead to poor utilization of active materials during cycling; and (3) the density distinction between sulfur (2.03 g cm^{-3}) and lithium sulfide (1.66 g cm^{-3}) causes uncontrollably strong volume expansion (up to 80%) during lithiation.[3]

To greatly overcome these challenges, numerous efforts have been made in terms of sulfur composites, electrolytes, lithium metal anodes, separators and multi-functional interlayers to improve the performance of Li–S batteries.[4–10] Among various studies, inserting a multifunctional interlayer of carbon materials such as multi-walled carbon nanotubes,[11] porous carbon,[12] and carbon fiber cloth[13] between the sulfur cathode and the PP separator has been proposed, which has been proved to be effective in enhancing the sulfur utilization and capturing polysulfides.[14,15] However, since there is no chemical affinity between non-polar carbon materials and polar polysulfides, the suppression ability towards the "shuttle effect" is inefficient during long-term discharging and charging cycles.[16] Therefore, some specific structures, which can form chemical interactions between carbon materials and polysulfides, should be designed to impede the dissolution of lithium polysulfides. Extensive studies have shown that many polar metal oxides (MnO_2,[17] TiO_2,[18] Co_3O_4,[19] V_2O_5[20] and Al_2O_3[21]) can form strong chemical bonds with lithium polysulfides to suppress the "shuttle effect" effectively. Particularly, MnO_2 is a promising functional material to capture and immobilize polysulfides due to its strong chemical absorption properties, which can greatly improve the performance of Li–S batteries.

Inspired by this point, carbon cloth (CC) decorated with MnO_2 nanosheet arrays (denoted as MCC) is developed as a bifunctional interlayer to inhibit the "shuttle effect" and promote the redox reaction kinetics. Carbon cloth was simply prepared by the carbonization of waste cotton cloth, and then used as a substrate to deposit MnO_2 nanosheets by a facile hydrothermal method (Fig. S1a, ESI†). This barrier layer of MnO_2 can form strong chemical absorption with polysulfides to suppress the "shuttle effect" (Fig. S1b, ESI†). Meanwhile, the dense carbon cloth matrix delivers a faster route for electron transfer and remarkably mitigates the volume expansion of the cathode.[22] As a result, the battery with MCC–PP delivers an initial discharge capacity of 843.4 mA h g^{-1} and maintains 682.6 mA h g^{-1} after 300 cycles at 1 C.

Fig. 1 exhibits the structures and phase compositions of our samples. As seen from Fig. 1a–c, the CC has a braided structure constituted by many hollow carbon fibers with a diameter of about 5 μm. The conductive carbon cloth matrix with a dense structure plays an important role in mitigating the volume expansion for sulfur as well as delivers a fast route for electron transfer. There may be some sizing resins on the surface of raw CC, while it became smoother after the acid oxidation for 12 h (Fig. S2, ESI†). After depositing MnO_2 on CC (Fig. 1d and e), we can observe numerous nanosheet arrays which uniformly grow on the CC, interlinking with each other and forming an ordered

Zhejiang Province key Laboratory of Quantum Technology and Device, Department of Physics, Zhejiang University, Hangzhou 310027, P. R. China. E-mail: miaowang@zju.edu.cn

† Electronic supplementary information (ESI) available. See DOI: 10.1039/d0ma00793e

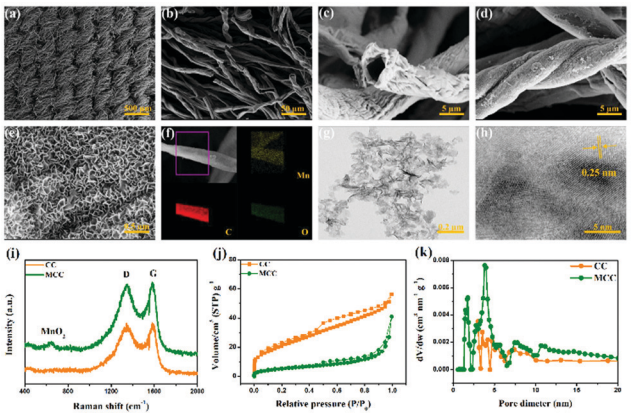

Fig. 1 Scanning electron microscopy (SEM) images of carbon cloth (a–c) and the MCC composite (d and e); elemental mapping images (f) of Mn, C, and O in the MCC composite; transmission electron microscopy (TEM) (g) and high resolution TEM (HRTEM) images (h) of MnO_2; (i) Raman spectra of CC and MCC composites; nitrogen adsorption–desorption isotherms (j) and pore size distributions (k) of CC and MCC composites.

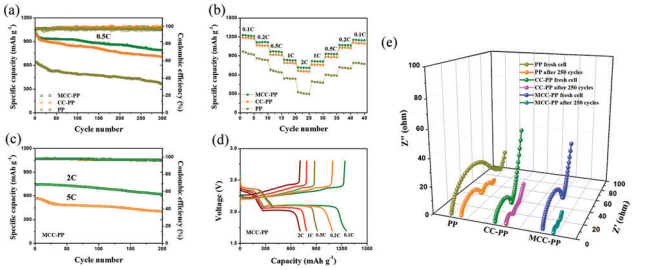

Fig. 2 Electrochemical characterization of batteries with different interlayers. (a) Cycling performances (0.5 C) and (b) rate capabilities of batteries with PP, CC–PP and MCC–PP; (c) cycling performances of batteries with MCC–PP at 2 C and 5 C; (d) initial galvanostatic charge–discharge profiles of batteries with MCC–PP at various current rates; (f) EIS curves of batteries with PP, CC–PP and MCC–PP.

arrangement. Energy dispersive spectroscopy (EDS) mapping of the MCC composites is depicted in Fig. 1f, demonstrating a uniform distribution of the Mn and O elements throughout the CC. The typical TEM and HRTEM images of MnO_2 obtained from MCC composites after intense ultrasonic vibration in ethyl alcohol for 5 h are presented in Fig. 1g and h. The MnO_2 nanosheets are thin and the lattice spacing is around 0.25 nm, well consistent with the (100) plane of the birnessite-type MnO_2 phase.[23] Fig. 1i discloses the Raman spectra of the CC and MCC composites. For CC, the two peaks exist at 1350.2 and 1581.9 cm^{-1} and are in accordance with the defected and graphitized carbon, indicating a D band and a G band, respectively. For MCC composites, there is a new peak originating from MnO_2 at about 650 cm^{-1}. Moreover, the I_D/I_G peak ratio of CC (0.96) increases to 1.02 after the deposition of MnO_2, interpreting that the sufficient disorders and defects can supply substantial active sites and strengthen the multi-electronic delivery.[24] The results of the nitrogen adsorption–desorption isotherms and the pore size distributions are shown in Fig. 1j and k. After the loading of MnO_2 on the CC, the Brunauer–Emmett–Teller (BET) surface area decreases from 73.1 $m^2\ g^{-1}$to 18.2 $m^2\ g^{-1}$. The pore size distribution of MCC is mainly in the range of 2–4 nm while the pore sizes of CC are mainly 3–5 nm. The distribution of MnO_2 can accelerate the redox reaction during operation, and at the same time the satisfactory surface area and the pore volume are vital for supplying ample active sites.

Crystalline structures of the CC and MCC compounds were determined through the X-ray diffraction patterns illustrated in Fig. S3a (ESI†). The two broad diffraction peaks of CC at 23.1° and 43.9° refer to the (002) and (100) planes of the amorphous carbon, respectively.[25] MCC composites display three new diffraction peaks at 12.0°, 25.2° and 37.3°, which are indexed to the (001), (002), and (111) planes, respectively, of birnessite-type MnO_2 (JCPDS no. 80-1098).[26] The (002) plane peak of MnO_2 shows weak intensity and overlaps with the diffraction peak of CC probably because of the lower loaded amount of MnO_2. The thermogravimetric analysis (TGA) curve was evaluated to obtain the weight ratio of MnO_2 on CC (Fig. S3b, ESI†), demonstrating that the MCC composites contain a loading mass for MnO_2 of about 38.57%. X-ray photoelectron spectroscopy (XPS) was employed to study the elemental compositions and functional groups of the MCC composites. The spectrum of the MCC composites presented in Fig. S4a (ESI†) exhibits three peaks at 642.1, 530.1 and 248.0 eV, corresponding to Mn, O and C, respectively.[27] The C 1s spectrum (Fig. S4b, ESI†) evidences three peaks at 284.5, 286.0 and 288.3 eV corresponding to C–C or C=C, C–O and C=O, respectively.[28] The spectrum of O 1s also shows three peaks located at 529.8 eV (C=O, Mn=O), 531.3 eV (C–OH) and 532.8 eV (C–O) (Fig. S4c, ESI†).[29]

Fig. 2 shows a comparison of the electrochemical performances of the batteries with PP, CC–PP and MCC–PP, respectively. As shown in Fig. 2a, the initial discharge capacity of the batteries with MCC–PP is 1013.6 mA h g^{-1} at 0.5 C, which is about the same as batteries with CC–PP (993.4 mA h g^{-1}) while evidently higher than those with PP (642.9 mA h g^{-1}), representing the contribution of the carbon cloth interlayer with a high conductivity in improving the charge transfer. After 300 cycles, the batteries with MCC–PP maintain a capacity of 788.6 mA h g^{-1} and a capacity retention rate of 77.85%. This retention capacity is higher than those of the batteries with CC–PP (662.8 mA h g^{-1}) and PP (362.7 mA h g^{-1}). Additionally, the batteries with MCC–PP possess a higher coulombic efficiency (98%), which remains almost unchanged after 300 cycles. Besides, from the morphologies and EDS detection signals (Fig. S5, ESI†), the anode surface of the batteries with MCC–PP is found to be smoother than other anodes with CC–PP and PP. The EDS detection signals indicate that the anode with PP expresses the strongest sulfur signal, while the anode with MCC–PP is detected by the weakest sulfur signal. This confirms that the MCC–PP interlayer is highly effective for suppressing the polysulfide migration during cycling. When the current rate increases to 1 C, as shown in Fig. S6 (ESI†), the batteries with MCC–PP still exhibit the best performance of an initial discharge capacity of 843.4 mA h g^{-1} and it remains at 682.6 mA h g^{-1} after 300 cycles with a lower capacity fading of 0.063% per cycle.

Importantly, the batteries with MCC–PP also show good cycling electrochemical performances even at large rates of 2 and 5 C, owing to the synergistic function of MnO_2 and CC in the absorption and re-utilization toward polysulfides (Fig. 2c). The rate performances of different batteries are illustrated in Fig. 2b. We can observe that the batteries with MCC–PP have much better rate capability than those with CC–PP and PP at current rates of 0.1, 0.2, 0.5, 1 and 2 C. Meanwhile, for the batteries with MCC–PP, the discharge capacities can nearly recover when the rate is restored, suggesting excellent stability and rate capabilities.

Typical discharge–charge profiles at different rates for the batteries with MCC–PP are displayed in Fig. 2d, and the curves present two typical voltage plateaus even at a large current density of 2 C, further revealing an excellent reversibility of the batteries with MCC–PP. The CV curves of the batteries are shown in Fig. S7 (ESI†). The curves exhibit two obvious reduction peaks in the cathode scan, which denote the conversion of sulfur to long-chain lithium polysulfides (Li_2S_n, $4 \leq n < 8$) and short-chain sulfide species (Li_2S_2, Li_2S).[11] In the anodic scan, the oxidation peak at about 2.4 V is attributed to the transformation from polysulfides to solid sulfur. Compared with the cells with PP and CC–PP, the one with MCC–PP displays a higher peak current and a lower anodic oxidation potential, which indicates the enhanced chemical reaction kinetics owing to the existence of manganese dioxide.

To further study the influence of different interlayers on the internal resistance, electrochemical impedance spectroscopy (EIS) tests were conducted (Fig. 2e). For the fresh cells, the R_{ct} values of cells with CC–PP (29 Ω) and MCC–PP (47 Ω) are evidently lower than those of the batteries with PP (83 Ω), demonstrating the positive efficacy of the high conductive carbon cloth interlayer for the charge transfer. However, the initial R_{ct} value of MCC–PP is slightly larger than that of CC–PP due to the lower conductive properties of MnO_2, which can be illustrated by the resistance measurements of CC and MCC (Fig. S8, ESI†). After 250 cycles at 0.2 C, the R_{ct} values of the batteries all significantly decrease since the active materials are well redistributed and contacted with the electrolyte, which accelerates the charge transfer.[30] The minimum R_{ct} value of MCC after cycling once more confirms the enhanced redox kinetics and the increased utilization of polysulfides due to the existence of MnO_2.

To intuitively observe the trapping ability of the MCC composites towards polysulfides, the adsorption test was researched (Fig. S9, ESI†). The Li_2S_6 solution containing MCC composites fades from yellow to light yellow after 12 h. By contrast, the solution containing CC shows no obvious color change compared to the blank Li_2S_6 solution, indicating the excellent adsorption ability of the MCC composites toward polysulfides. MCC composites with or without the adsorption test were characterized by XPS. For the pristine MCC composites (Fig. 3a), the Mn $2p_{3/2}$ spectrum exhibits an Mn^{2+} peak at 640.6 eV. Obviously, we can see a maximum peak at 642.1 eV which results from the Mn^{4+} valent state as an emergence of characteristic multiplet and agrees with the two satellite peaks at 643.4 and 644.9 eV.[28] In contrast, the MCC composites after

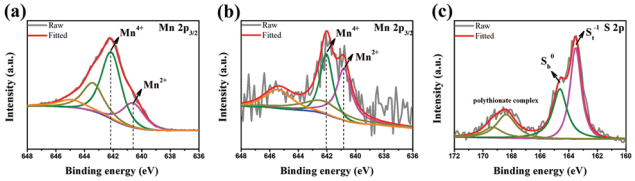

Fig. 3 Mn $2p_{3/2}$ XPS spectra of MCC composites (a) before and (b) after soaking tests; (c) the S 2p XPS spectrum of MCC composites after the soaking tests.

permeation tests exhibit an enhanced signal from the Mn^{2+} ions located at 640.8 eV, accompanied by the decreased contribution from the Mn^{4+} ions, which may be the redox reaction between Mn^{4+} and Li_2S_6 (Fig. 3b). For the S 2p spectrum of MCC-Li_2S_6 (Fig. 3c), there exists two peaks at 163.5 eV and 164.6 eV, which can be attributed to the terminal (S_t^{-1}) and bridging sulfur (S_b^0) atoms, respectively.[31] The other two peaks at 168.4 and 169.3 eV are consistent with the polythionate complex, implying the interaction and strong chemical bonds between MnO_2 and polysulfides.[19] At the same time, the peaks of S_t^{-1} and S_b^0 for MCC-Li_2S_6 are both higher than those of CC-Li_2S_6, corresponding to the strong chemical interaction between MnO_2 and Li_2S_6.[32]

In summary, a multifunctional CC interlayer decorated with MnO_2 nanosheets is successfully designed to improve the performances effectively of Li–S batteries. The conductive CC serves as a physical barrier and provides a fast pathway for electron transportation. MnO_2 can form chemical bonding with polysulfides, which can capture the polysulfide intermediates from the cathode and significantly favor the recycling of active materials. A significantly improved performance of capacity, rate and cycling stability for Li–S batteries with MCC–PP is accomplished. A retained capacity of 682.6 mA h g^{-1} is achieved after 300 cycles with a capacity decay of only 0.063% per cycle at 1 C. This work may offer some new insights into the designs to inhibit the shuttle effect, which can contribute to the multifunctional interlayer in-depth studies of advanced-performance rechargeable batteries.

Author contributions

Huayun Liu: methodology, investigation, software, and writing-draft. Hao Cheng: validation, formal analysis, visualization, writing-review, and data curation. Han Jin: validation, formal analysis, and writing-editing. Cheng Gao: data curation. Peng Zhang: writing-review and writing-editing. Miao Wang: resources, writing-review, writing-editing, and supervision.

Conflicts of interest

There are no conflicts to declare.

Acknowledgements

This work was financially supported by the National Natural Science Foundation of China (Grant No. 61471317).

Notes and references

1 P. G. Bruce, S. A. Freunberger, L. J. Hardwick and J.-M. Tarascon, *Nat. Mater.*, 2012, **11**, 19–29.
2 Y.-X. Yin, S. Xin, Y.-G. Guo and L.-J. Wan, *Angew. Chem., Int. Ed.*, 2013, **52**, 13186–13200.
3 B. L. Ellis, K. T. Lee and L. F. Nazar, *Chem. Mater.*, 2010, **22**, 691–714.
4 M. S. Whittingham, *Chem. Rev.*, 2004, **104**, 4271–4301.
5 S. S. Zhang, *J. Power Sources*, 2013, **231**, 153–162.
6 L. Suo, Y.-S. Hu, H. Li, M. Armand and L. Chen, *Nat. Commun.*, 2013, **4**, 1481.
7 K. Yan, Z. Lu, H.-W. Lee, F. Xiong, P.-C. Hsu, Y. Li, J. Zhao, S. Chu and Y. Cui, *Nat. Energy*, 2016, **1**, 16010.
8 Y.-X. Yao, X.-Q. Zhang, B.-Q. Li, C. Yan, P.-Y. Chen, J.-Q. Huang and Q. Zhang, *InfoMat*, 2020, **2**, 379–388.
9 Y. Liang, C.-Z. Zhao, H. Yuan, Y. Chen, W. Zhang, J.-Q. Huang, D. Yu, Y. Liu, M.-M. Titirici, Y.-L. Chueh, H. Yu and Q. Zhang, *InfoMat*, 2019, **1**, 6–32.
10 B.-Q. Li, L. Kong, C.-X. Zhao, Q. Jin, X. Chen, H.-J. Peng, J.-L. Qin, J.-X. Chen, H. Yuan, Q. Zhang and J.-Q. Huang, *InfoMat*, 2019, **1**, 533–541.
11 Y.-S. Su, Y. Fu, T. Cochell and A. Manthiram, *Nat. Commun.*, 2013, **4**, 2985.
12 Y. Zhong, X. Xia, S. Deng, J. Zhan, R. Fang, Y. Xia, X. Wang, Q. Zhang and J. Tu, *Adv. Energy Mater.*, 2018, **8**, 1701110.
13 Q. Pang, X. Liang, C. Y. Kwok and L. F. Nazar, *Nat. Energy*, 2016, **1**, 16132.
14 Z. Wei, Y. Ren, J. Sokolowski, X. Zhu and G. Wu, *InfoMat*, 2020, **2**, 483–508.
15 C. Zhang, L. Cui, S. Abdolhosseinzadeh and J. Heier, *InfoMat*, 2020, **2**, 613–638.
16 H. Tang, W. Li, L. Pan, K. Tu, F. Du, T. Qiu, J. Yang, C. P. Cullen, N. McEvoy and C. Zhang, *Adv. Funct. Mater.*, 2019, **29**, 1901907.
17 Z. Li, J. Zhang and X. W. Lou, *Angew. Chem., Int. Ed.*, 2015, **54**, 12886–12890.
18 Z. Xiao, Z. Yang, L. Wang, H. Nie, M. E. Zhong, Q. Lai, X. Xu, L. Zhang and S. Huang, *Adv. Mater.*, 2015, **27**, 2891–2898.
19 J. Pu, Z. Shen, J. Zheng, W. Wu, C. Zhu, Q. Zhou, H. Zhang and F. Pan, *Nano Energy*, 2017, **37**, 7–14.
20 W. Li, J. Hicks-Garner, J. Wang, J. Liu, A. F. Gross, E. Sherman, J. Graetz, J. J. Vajo and P. Liu, *Chem. Mater.*, 2014, **26**, 3403–3410.
21 Z. Zhang, Y. Lai, Z. Zhang, K. Zhang and J. Li, *Electrochim. Acta*, 2014, **129**, 55–61.
22 H. Tang, W. Li, L. Pan, C. P. Cullen, Y. Liu, A. Pakdel, D. Long, J. Yang, N. McEvoy, G. S. Duesberg, V. Nicolosi and C. Zhang, *Adv. Sci.*, 2018, **5**, 1800502.
23 X. Liang, C. Hart, Q. Pang, A. Garsuch, T. Weiss and L. F. Nazar, *Nat. Commun.*, 2015, **6**, 5682.
24 L. Peng, Y. Liang, H. Dong, H. Hu, X. Zhao, Y. Cai, Y. Xiao, Y. Liu and M. Zheng, *J. Power Sources*, 2018, **377**, 151–160.
25 S. He and W. Chen, *J. Power Sources*, 2015, **294**, 150–158.
26 A. Boisset, L. Athouel, J. Jacquemin, P. Porion, T. Brousse and M. Anouti, *J. Phys. Chem. C*, 2013, **117**, 7408–7422.
27 L. Ni, G. Zhao, G. Yang, G. Niu, M. Chen and G. Diao, *ACS Appl. Mater. Interfaces*, 2017, **9**, 34793–34803.
28 X. Wang, G. Li, J. Li, Y. Zhang, A. Wook, A. Yu and Z. Chen, *Energy Environ. Sci.*, 2016, **9**, 2533–2538.
29 S. Yuan, Z. Guo, L. Wang, S. Hu, Y. Wang and Y. Xia, *Adv. Sci.*, 2015, **2**, 1500071.
30 X. Li, Q. Zhu, W. Guo and Q. Lu, *J. Electroanal. Chem.*, 2019, **840**, 144–152.
31 S. Rehman, T. Tang, Z. Ali, X. Huang and Y. Hou, *Small*, 2017, **13**, 1700087.
32 Y. Wei, Y. Tao, C. Zhang, J. Wang, W. Qiao, L. Ling and D. Long, *Electrochim. Acta*, 2016, **188**, 385–392.